Journal of Computational Physics 317 (2016) 347–361

Contents lists available at ScienceDirect

Journal of Computational Physics

www.elsevier.com/locate/jcp

Surface-tension-driven Stokes flow: A numerical method based on conformal geometry

Peter Buchak *, Darren G. Crowdy

Department of Mathematics, Imperial College London, 180 Queen's Gate, London, SW7 2AZ, United Kingdom

ARTICLE INFO

Article history:
Received 10 January 2015
Received in revised form 16 October 2015
Accepted 21 April 2016
Available online 25 April 2016

Keywords:
Stokes flow
Free surface
Surface tension
Conformal mapping
Numerical method

ABSTRACT

A novel numerical scheme is presented for solving the problem of two dimensional Stokes flows with free boundaries whose evolution is driven by surface tension. The formulation is based on a complex variable formulation of Stokes flow and use of conformal mapping to track the free boundaries. The method is motivated by applications to modelling the fabrication process for microstructured optical fibres (MOFs), also known as "holey fibres", and is therefore tailored for the computation of multiple interacting free boundaries. We give evidence of the efficacy of the method and discuss its performance.

1. Introduction

The topic of this paper is two dimensional free surface Stokes flow driven by surface tension on its boundaries. While, at first sight, the two dimensionality of the problem might appear to render it of little practical or physical significance, it turns out that it plays a crucial role in a wide variety of low Reynolds number flow situations in the glass industry where thin threads, fibres and capillaries are fabricated by means of a drawing technique involving slender viscous fluid threads. Under a natural asymptotic approximation based on that slenderness, the two dimensional free surface Stokes flow problem considered here arises naturally in the mathematical models, often "decoupled" to a large extent from a very different physics occurring in the transverse, or axial, "pulling" direction. It is therefore a problem worthy of detailed investigation.

Actually, much theoretical and numerical work has been done on this free boundary problem over the past several decades, much of it motivated by the study of so-called "viscous sintering". In this process, a granular material is heated causing adjacent particles to coalesce under the effects of surface tension. Most studies have focused on so-called "unit problems", as a first step in developing "a phenomenological theory for macroscopic systems" [18]. And although the surface-tension-driven Stokes flow problem is a highly nonlinear free boundary problem, even in two dimensions, it is remarkable that several exact solutions to it are known for special planar geometries [11,26,31,7,4,5]. For general initial conditions, however, and especially for general multiply connected domains, numerical methods must be used. The existence of non-trivial exact solutions (even for multiply connected geometries [4]) is, nevertheless, a significant advantage in providing non-trivial quantitative tests for numerical schemes.

Without exception, the derivation of exact solutions to this problem relies on a complex variable reformulation of the problem and use of the powerful results of analytic function theory, including conformal mappings, to provide closed-form

* Corresponding author.
E-mail addresses: peter.buchak@gmail.com (P. Buchak), d.crowdy@imperial.ac.uk (D.G. Crowdy).

http://dx.doi.org/10.1016/j.jcp.2016.04.044

descriptions of the time-evolving interfaces. The nature of all the known exact solutions is that the functional form of an initial conformal mapping is *preserved* under evolution; this implies that it is necessary only to track the evolution of a finite set of time-evolving parameters appearing in these mappings in order to determine the free surface evolution. Given the central role played by complex analysis in the exact solution schemes, it seemed to us to be appropriate to explore the formulation of *numerical* schemes based on that same mathematical approach. This is the topic of the present paper.

The first numerical studies of surface tension driven Stokes flows made use of finite element methods [27,13,14]. However, because inertia is neglected in Stokes flow, it is only necessary to track the evolution of the free boundary and boundary integral methods have become the preferred approach. Kuiken [18] was one of the earliest expositors of these methods; an array of related numerical studies soon followed [1,34,33,22–24], including for multiply connected domains having more than one boundary [32,25]. A drawback of many of these methods was that regions of high curvature in the interface can cause difficulties. Kuiken acknowledged that "initial shapes showing more extreme curvature gradients... cannot be dealt with by the boundary-element method in its present form" [18]. Van de Vorst and Mattheij [33] noted that the problem is ill-conditioned when the contact surfaces of the particles are small, requiring a special algorithm for redistributing nodes along the boundary. A significant advantage of describing free interfaces using conformal mappings is that they can be ideally suited to high curvature regions. Indeed, several of the known exact solutions [11,5] describe the surface tension driven "smoothing" of near-touching circular discs which typically involve isolated regions of very high curvature.

Stokes flow problems have already been addressed using complex variables. Greengard, Kropinski, and Mayo [9] have described a boundary integral method based on a complex variable formulation and have formulated it to tackle regions of arbitrary connectivity. In contrast to the free-boundary problem we consider, these authors focused on problems where the velocity is specified on fixed boundaries. A boundary integral method for the free-boundary problem was introduced by Kropinski [17] and improved by Ojala and Tornberg [21]. Chakravarthy and Chiu [3] used a boundary integral method to address the same problem that has motivated us (see §2) – the fabrication of so-called microstructured optical fibres (or MOFs) – and they also allow for free boundaries and multiply connected regions. These studies make use of the Sherman–Lauricella integral representation of the solution of the biharmonic equation that is perhaps more familiar in the study of plane elasticity [20]. The previous work which is closest in spirit to ours is the numerical approach to studying surfactant effects in two dimensional free surface Stokes flow due to Siegel [28,29] which focused on simply connected fluid domains. Those methods also make use of a complex variable formulation combined with a conformal mapping description of the boundary. Our approach is its natural generalization to more complicated, multiply connected domain types.

Complex variable methods may initially appear restrictive in that they can only be used for two dimensional problems. However, a significant advantage becomes clear when one considers the curvature term in the dynamic boundary condition (equation (2) to follow). Computing the curvature requires two spatial derivatives, with respect to arclength, of a boundary parametrization (d^2z/ds^2, in complex notation, where s is arclength). However, it will be seen below that a complex formulation of the dynamic boundary condition (6) can be integrated once with respect to s, resulting in an equation that involves only first arclength derivatives (i.e., dz/ds). Thus, because complex variable methods are based on the tangent to the boundary rather than its curvature, they lead to equations that can in theory be solved more accurately and with less severe time stepping constraints when high curvature regions of a boundary are present. The difficulties associated with the curvature have been noted before by other researchers, beginning with Hou, Lowengrub, and Shelley [12], who introduced a formulation to remove the stiffness associated with this term for the problems of free surfaces in Hele-Shaw and inviscid flow. The complex variable representation used here has the advantage that the second derivative is eliminated by an integration that arises naturally, without requiring special attention to this problem.

Conformal mapping may appear to offer no practical benefit over boundary integral methods. However, it does conveniently solve some problems that plague these methods. In systems where *compressible* bubbles arise, even in two dimensional flows, the standard boundary integral formulations of Stokes flow suffer from certain mathematical problems such as the appearance of hypersingular integrals in the standard formulation [23] (see also [24]). In addition, for boundaries with regions of high curvature, boundary integral methods must take special steps to ensure that the boundary points remain properly distributed. For instance, this motivated Kropinski [17] to develop a technique for choosing the tangential velocity that ensures the points remain equally spaced. Conformal mapping circumvents both of these complications.

In this paper, we therefore describe a novel numerical approach to the Stokes flow free boundary problem based on the very concepts of complex analysis and conformal mapping on which the exact solution structure is based. It can be used to compute solutions for initial conditions for which exact solutions are not known. It appears to circumvent many of the numerical difficulties, just described above, associated with alternative schemes, such as the standard boundary integral formulations of Stokes flow for compressible bubbles. A second reason for our work is that the exact solutions for compressible bubbles given by [4] lie at the heart of the so-called "elliptical pore model" recently presented in [2] and devised for the purposes of modelling the fabrication process for optical fibres without the need for full numerical simulations. Indeed the numerical scheme of this paper was devised for the purposes of testing our recent modelling work on the drawing of microstructured optical fibres [2]. A brief outline of this application is described next.

2. Application to microstructured optical fibres

Microstructured optical fibres, or MOFs, are a relatively new breed of optical fibres where light is guided by the geometry of an array of channels, or "holes", running along the length of the fibre and whose geometry affects the light transmission

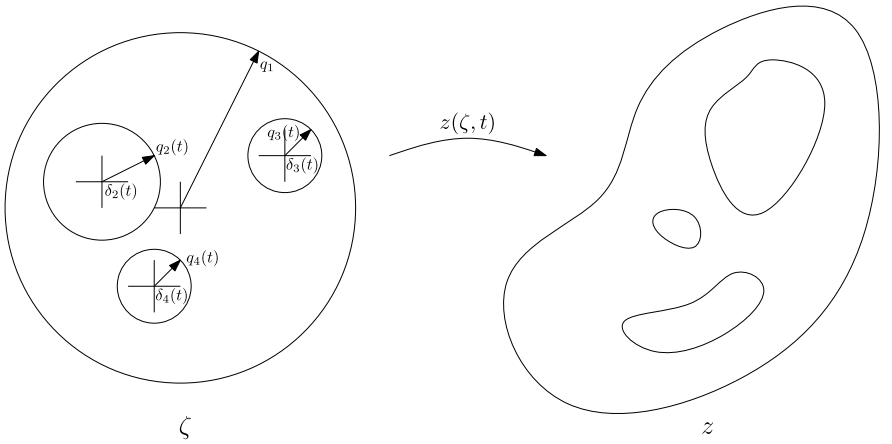

Fig. 1. The numerical method computes the evolution of the conformal map from a multiply connected circular region in a parametric ζ plane (left) to a typical fluid region in the z plane (right). The map $z(\zeta,t)$, as well as the centers $\delta_m(t)$ and radii $q_m(t)$ of the circles in the preimage domain, change as the shape of the fluid region evolves in time and must be determined.

properties in ways that can be adapted by appropriately tailoring the geometry of those channels [15]. The modelling approach adopted by the authors in [30] rests on two key observations. For slender fibres, the three-dimensional fibre drawing problem splits into two simpler problems, a one-dimensional problem in the axial direction (the "stretching" problem) and a two-dimensional problem in the cross-plane (the "sintering" problem) [6]; it is the latter problem that forms the focus of the present article. As noted in [6], the cross-plane problem in fibre drawing turns out to be simply the "classical two-dimensional Stokes flow free-boundary problem" driven by surface tension, with unit surface tension, area, and viscosity, evolving with respect to a "reduced time" variable τ. This motivated our efforts to devise a fast, easy-to-implement method for solving this problem numerically for arbitrary multiply connected cross-plane geometries. The structured cross section in microstructured fibres requires a method capable of dealing quickly and effectively with multiply connected regions with free boundaries. Recently, a so-called "elliptical pore model" has been introduced [2] aimed at accurately approximating the solution to the two dimensional surface-tension-driven Stokes flow problem in the case where the region is a circular disc with a finite number of well separated elliptical holes. It is for the purposes of testing this approximate model against full numerical simulations that the method of this paper was devised.

3. Complex variable formulation

Consider slow viscous flow in a time-evolving fluid region $D(t)$ governed by the Stokes equations,

$$\begin{aligned} -\nabla p + \mu\nabla^2\vec{u} &= 0 \\ \nabla\cdot\vec{u} &= 0, \end{aligned} \tag{1}$$

where $\vec{u}(x,y,t)$ is the fluid velocity, $p(x,y,t)$ is the pressure, and μ is the viscosity, uniform in the fluid region. It is required to solve for the evolution in time t of the fluid region $D(t)$. On the right in Fig. 1 a typical (quadruply connected) fluid region is shown; in addition to the outer boundary it has three internal closed boundaries. On the m-th free boundary, surface tension acts and an external pressure p_m is imposed so the dynamic and kinematic boundary conditions are given, respectively, by

$$-pn_i + 2\mu\epsilon_{ij}n_j = -\gamma\kappa n_i - p_m n_i, \tag{2}$$

$$\frac{d\vec{x}}{dt}\cdot\vec{n} = \vec{u}\cdot\vec{n}. \tag{3}$$

Each boundary can be described by a closed curve $\vec{x}(s,t)$ where the arclength s is used as the natural parameter. $\epsilon_{ij}(x,y,t)$ is the rate-of-strain tensor, $n_i(s,t)$ the unit normal, $\kappa(s,t)$ the curvature, and γ the surface tension coefficient. For fibre drawing, the cross-plane problem is to be solved with $\mu=\gamma=1$. For other applications, the constants μ and γ can be eliminated from the equations and boundary conditions by scaling lengths by some characteristic length L, pressures by γ/L, and time by $\mu L/\gamma$. This allows the problem to be solved in complete generality with μ and γ set to 1, which we do here.

For two dimensional incompressible Stokes flow it is possible to describe the flow in terms of a stream function $\psi(x,y,t)$ satisfying the biharmonic equation [19,31],

$$\nabla^4\psi = 0. \tag{4}$$

Introducing the complex variable $z = x + \mathrm{i}y$, the general solution to (4) can be written [19]

$$\psi = \Im[\overline{z} f(z,t) + g(z,t)],$$

where f and g are two functions that are analytic in the fluid. They also depend on time because $D(t)$ is evolving in time, but they are determined instantaneously by the current shape of the fluid domain (the flow is "quasi-steady"). The fluid velocity, pressure, vorticity, and rate-of-strain tensor are given in terms of f and g by [19,4]

$$\begin{aligned} u + \mathrm{i}v &= -f(z,t) + z\overline{f'(z,t)} + \overline{g'(z,t)} \\ p - \mathrm{i}\omega &= 4f'(z,t) \\ \epsilon_{11} + \mathrm{i}\epsilon_{12} &= z\overline{f''(z,t)} + \overline{g''(z,t)}. \end{aligned} \tag{5}$$

Here, primes indicate derivatives with respect to z.

It can be verified that the fluid stress on a boundary, $-pn_i + 2\epsilon_{ij}n_j$, is given by

$$2\mathrm{i}\left(\frac{\partial H}{\partial z}\frac{dz}{ds} + \frac{\partial H}{\partial \overline{z}}\frac{d\overline{z}}{ds}\right)$$

where we define

$$H(z,\overline{z},t) \equiv f(z,t) + z\overline{f'(z,t)} + \overline{g'(z,t)}.$$

The fluid stress on the left hand side of (2) is therefore recognized to be a total derivative with respect to arclength s. Likewise, in complex notation, the curvature and pressure terms on the right hand side of (2) are d^2z/ds^2 and $\mathrm{i}p_m dz/ds$, respectively, and these are also total s derivatives. (2) can therefore be integrated along each boundary, resulting in an equation involving only *first* derivatives with respect to s. This feature reduces any time-stepping constraints and mollifies any stiffness associated with regions of high curvature in the fluid interfaces. With some minor manipulation, the dynamic (2) and kinematic (3) boundary conditions on boundary m become

$$f(z,t) + z\overline{f'(z,t)} + \overline{g'(z,t)} - A_m(t) = -\frac{\mathrm{i}}{2}\frac{dz}{ds} + \frac{1}{2}p_m z, \tag{6}$$

$$\Re\left\{\frac{dz}{dt}\mathrm{i}\frac{\overline{dz}}{ds}\right\} = \Re\left\{\left(-f(z,t) + z\overline{f'(z,t)} + \overline{g'(z,t)}\right)\mathrm{i}\frac{\overline{dz}}{ds}\right\}. \tag{7}$$

The functions $A_m(t)$ arise from integration of each boundary condition with respect to arclength and must be found as part of the solution. It should be noted that the left hand side of the dynamic boundary condition is simply $H(z,\overline{z},t) - A_m(t)$.

The total force on an enclosed bubble is the integral, with respect to s, of $2\mathrm{i}dH/ds$ around that boundary. But from (6) it is clear that H is single-valued around each bubble so there is no net force on any of the enclosed bubbles. As a result, $f(z,t)$ and $g'(z,t)$ are single-valued functions in the fluid region.

4. Conformal mapping approach

To track the evolution of the fluid boundaries, we introduce a time-dependent conformal mapping $z(\zeta,t)$ from a canonical circular region in the complex ζ-plane to the evolving fluid region as illustrated in Fig. 1. Note that we will use z to denote both the physical variable and the conformal mapping function, but this should not cause confusion. The Riemann mapping theorem [8] guarantees that the shape of any bounded region with $M-1$ arbitrarily shaped holes can be represented as the image under such a conformal map of the interior of the disk $|\zeta - \delta_1(t)| = q_1(t)$ with $M-1$ circular holes $|\zeta - \delta_m(t)| = q_m(t)$ $(m = 2,\ldots,M)$. Because a conformal map to a given region only exists for a specific configuration of circles, their centers $\delta_m(t) \in \mathbb{C}$ and radii $q_m(t) \in \mathbb{R}$ evolve in time. The evolution of these so-called *conformal moduli* must be found as part of the solution. For definiteness, we take $\delta_1(t) = 0$ and $q_1(t) = 1$. A discussion of the remaining degrees of freedom in this conformal mapping description is given in (§8).

With such a map defined, we can introduce

$$F(\zeta,t) \equiv f(z(\zeta,t),t), \qquad G(\zeta,t) \equiv g'(z(\zeta,t),t). \tag{8}$$

In terms of these the dynamic and kinematic boundary conditions (6), (7) in the ζ plane are

$$F(\zeta,t) + \frac{z(\zeta,t)}{z'(\zeta,t)}\overline{F'(\zeta,t)} + \overline{G(\zeta,t)} - A_m(t) = -\frac{\mathrm{i}}{2}\frac{dz}{ds} + \frac{1}{2}p_m z(\zeta,t), \tag{9}$$

where $z'(\zeta,t)$ denotes $\partial z/\partial\zeta$, and

$$\Re\left\{\frac{dz}{dt}\mathrm{i}\frac{\overline{dz}}{ds}\right\} = \frac{1}{2} + \Re\left\{\left(-2F(\zeta,t) + \frac{1}{2}p_m z(\zeta,t) + A_m(t)\right)\mathrm{i}\frac{\overline{dz}}{ds}\right\}, \tag{10}$$

where the unit tangent vector, in terms of the conformal mapping, is

$$\frac{dz}{ds} = \begin{cases} \dfrac{\mathrm{i}(\zeta - \delta_m)z'(\zeta,t)}{q_m|z'(\zeta,t)|}, & m = 1, \\ -\dfrac{\mathrm{i}(\zeta - \delta_m)z'(\zeta,t)}{q_m|z'(\zeta,t)|}, & m \geq 2, \end{cases} \tag{11}$$

with the sign chosen to keep the fluid region to the left as each boundary component is traversed. Note that (6) has been used to simplify the right hand side of (10).

At each instant $F(\zeta,t)$ and $G(\zeta,t)$ and $\{A_m(t)\}$ satisfying (9) can be found. In turn, these enter the kinematic condition (10) to determine the evolution of the fluid. As the fluid region evolves, both the map $z(\zeta,t)$ and the radii $q_m(t)$ and locations $\delta_m(t)$ of the circles in the preimage domain change. In our implementation, these are updated using a fourth order Runge–Kutta time-stepping scheme applied to (10).

Our method requires an initial map $z(\zeta,0)$ and initial preimage domain parameters $q_m(0)$ and $\delta_m(0)$. For problems where the initial configuration is specified but no map is given, a preimage domain and a mapping from that domain must first be found. Constructing conformal mappings is an area of active research and an extensive history and multifarious methods are available to compute mappings to arbitrary regions. Here we have made use of a generalized Fornberg-type method for conformal mapping of multiply connected domains recently revised by Kropf [16].

5. Existence and uniqueness

In this section we suppress dependence of all quantities on t. Stokes flow that does not contain any singularities is unable to exert a net torque around its boundary. Writing ∂D to denote the entire (directed) boundary of the fluid region, and making use of the single-valuedness of H,

$$0 = \oint_{\partial D} \vec{r} \times \vec{F}\, ds = \Re \oint_{\partial D} 2\mathrm{i}\frac{dH}{ds}(-\mathrm{i}\overline{z})\, ds = -2\Re \oint_{\partial D} H\, d\overline{z}. \tag{12}$$

As a consequence, solutions to free boundary Stokes flow problems only exist when the forcing also satisfies a condition of zero torque. For our problem, driven by surface tension and pressure, the right hand side of (9) always satisfies this condition. This can be seen by evaluating the torque on ∂D,

$$\Re \oint_{\partial D} \left(-\frac{\mathrm{i}}{2}\frac{dz}{ds} + \frac{1}{2}p_m z \right) d\overline{z} = 0. \tag{13}$$

Thus, a solution always exists.

The solutions satisfying the dynamic boundary condition (9) are not unique, however. Additional constraints must be imposed to enforce uniqueness on the Goursat representation for the flow. To see this note that the transformations

$$\begin{aligned} f(z) &= \tilde{f}(z) + B + Q + \mathrm{i}Rz, \\ g(z) &= \tilde{g}(z) + C + \overline{B}z - \overline{Q}z, \\ A_m &= \tilde{A}_m + 2B, \end{aligned} \tag{14}$$

where $B, C, Q \in \mathbb{C}$ and $R \in \mathbb{R}$ are constants, leaves the left hand side of (9) unchanged. Complex constants B and C reflect the nonuniqueness of the Goursat representation (they leave the velocity and pressure fields unchanged [19][1]); Q and R reflect the indeterminacy associated with a translation and rotation. For the problem in the ζ plane, this transformation is

$$\begin{aligned} F(\zeta) &= \tilde{F}(\zeta) + F_0 + \mathrm{i}Rz(\zeta), \\ G(\zeta) &= \tilde{G}(\zeta) + G_0, \\ A_m &= \tilde{A}_m + F_0 + \overline{G}_0, \end{aligned} \tag{15}$$

where $F_0 = B + Q$ and $G_0 = \overline{B} - \overline{Q}$ are complex constants, for a total of five real degrees of freedom.

As for the kinematic boundary condition (10) it is necessary to take account of the three real degrees of freedom in the Riemann mapping theorem and, in particular, to impose conditions that render the conformal mapping function unique. The particular choices we make will be discussed later.

[1] Langlois uses a different convention for the Goursat functions and gives an additional term in the transformation for $f(z)$. In our notation, this term is Az, where A is real. Addition of this term leaves the velocity field unchanged but adds a constant to the pressure.

6. Series representation

It is well-known that any function $h(\zeta)$ that is analytic *and* single-valued in the multiply connected circular domain shown in Fig. 1 can be represented as a series of the form

$$h(\zeta) = \sum_{m=1}^{M} \sum_{n} \left(\frac{\zeta - \delta_m}{q_m} \right)^n h_{m,n}, \tag{16}$$

where the coefficients have the integral expressions

$$h_{m,n} = \frac{1}{2\pi \mathrm{i}} \oint_{|\zeta' - \delta_m| = q_m} q_m^n (\zeta' - \delta_m)^{-(n+1)} h(\zeta')\, d\zeta' \approx \frac{1}{K} \sum_{k=0}^{K-1} e^{-2\pi \mathrm{i} n k/K} h(\delta_m + q_m e^{2\pi \mathrm{i} k/K}). \tag{17}$$

Here, n ranges from 0 to ∞ for the outer boundary and from -1 to $-\infty$ for the inner boundaries. This representation follows directly from Cauchy's integral formula. The factors of q_m have been absorbed into the coefficients to prevent overflow for large $|n|$. It is evident that the coefficients $h_{m,n}$ can be evaluated by a Fast Fourier Transform (FFT) given the values of $h(\zeta)$ on the boundaries. In practice, we truncate the series associated with each boundary m at N_m terms, so that n ranges from 0 to $N_1 - 1$ for the outer boundary and from -1 to $-N_m$ for inner boundary m.

When, at each instant, $z(\zeta, t)$, $F(\zeta, t)$, and $G(\zeta, t)$ are represented in the form (16), and the dynamic boundary condition (9) is expanded in powers of $\eta = (\zeta - \delta_m)/q_m$ on each boundary, it becomes a linear system of equations for the coefficients of $F(\zeta, t)$ and $G(\zeta, t)$ and the instantaneous values of $\{A_m(t)\}$. If the conformal map $z(\zeta, t)$ is written as

$$z(\zeta, t) = \sum_{m=1}^{M} \sum_{n} \left(\frac{\zeta - \delta_m(t)}{q_m(t)} \right)^n a_{mn}(t) \tag{18}$$

then the kinematic boundary condition (10) becomes a linear system of equations for the time derivatives of the set $\{a_{mn}(t), q_m(t), \delta_m(t)\}$.

We have ensured the satisfaction of the boundary conditions (9), (10) by equating powers of $\eta = (\zeta - \delta_m)/q_m$ in the Laurent series on each boundary m. The products that appear in the boundary conditions are taken coefficient-wise. We find that accuracy is improved by using up to twice the number of powers for the products on a boundary as we equate on that boundary. Because neither boundary condition has a unique solution, and in addition the dynamic boundary condition trivially satisfies equation (12), the matrices for both systems of equations, as stated, would be singular. To prevent this, the systems must be modified by the removal of certain equations and unknowns. Provided this is done properly, and provided the number of powers equated on each boundary is chosen carefully, a square system of equations results. This is discussed in detail in the following two sections.

7. Solving for the instantaneous flow field

In this section we consider finding $F(\zeta, t)$, $G(\zeta, t)$, and $\{A_m(t)\}$ satisfying (9) at some fixed instant t. The dynamic boundary condition (9) is a linear system of equations for $\sum_m N_m$ complex coefficients of $F(\zeta, t)$, $\sum_m N_m$ complex coefficients of $G(\zeta, t)$, and M complex constants A_m. If $F(\zeta, t)$ and $G(\zeta, t)$ contain powers up to $\eta^{\pm N}$ on boundary m, it can be seen that the left hand side of the dynamic boundary condition will contain powers η^{-N} through η^N. Therefore, on the outer boundary, we equate the complex Laurent coefficients for powers $-N_1 + 1$ through $N_1 - 1$, while on inner boundary m, we equate the complex Laurent coefficients for powers $-N_m$ through N_m. This complex system is equivalent to a real linear system of $4\sum_m N_m + 2M - 4$ equations for the $4\sum_m N_m + 2M$ real and imaginary parts of the unknowns. The discrepancy between the numbers of rows and columns suggests that there are further constraints that must be taken into account.

The dynamic boundary condition can be thought of as a mapping from a set of flow fields to a set of corresponding boundary forces. Usually, there is a one-to-one correspondence between flow fields and boundary forces, but this is not true for free boundary problems: different flow fields can produce the same boundary forces, and only some of the possible configurations of boundary forces can be produced at all. This means that the dynamic boundary condition must be treated with some care.

(12) states that the net torque exerted on the boundaries must vanish. Writing this integral over the boundaries $\zeta = \delta_m + q_m \eta$ in the ζ plane, and subtracting the quantities $A_m(t)$ from the integrand, (12) becomes

$$0 = \Re \sum_m \pm q_m(t) \oint_{|\eta| = 1} \eta^{-2} \overline{z'(\zeta, t)} (H(\zeta, \overline{\zeta}, t) - A_m(t))\, d\eta, \tag{19}$$

with the positive sign taken on the outer boundary and the negative sign taken on the inner boundaries. (19) is a single real condition on $H - A_m$, the left hand side of the dynamic boundary condition (9). It expresses a relationship between the coefficients of this quantity, and therefore between the equations of the linear system representing (9). To make the

equations independent, one of the equations appearing in the relationship (19) must be eliminated. The details of our implementation are given in Appendix A.

Because the solution of the dynamic boundary condition is not unique, five real unknowns must be eliminated, corresponding to the real and imaginary parts of F_0 and G_0 and R in (15). To fix F_0, we set $F_{1,0} = 0$. To fix G_0, we set $G_{1,0} = 0$. To fix R, we could set to zero any real or imaginary part of another coefficient of $F(\zeta, t)$ in which $\mathrm{i}z(\zeta, t)$ appears; we choose this coefficient by finding the coefficient of $\mathrm{i}z(\zeta, t)$ with maximum absolute real or imaginary part.

After eliminating one equation and five unknowns, we arrive at a square, invertible system of $4\sum_m N_m + 2M - 5$ real equations and unknowns. The case of a circular fluid region affords useful insights into the elimination of equations and unknowns and is discussed in Appendix B.

8. Updating the domain shape

Having fixed $\delta_1(t) = 0$ and $q_1(t) = 1$, the kinematic boundary condition (10) is a linear system of equations for $\sum_m N_m$ complex coefficients $dz_{m,n}/dt$, $M - 1$ complex values $d\delta_m/dt$, and $M - 1$ real values dq_m/dt. On the outer boundary, the series for $m = 1$ for dz/dt contains powers of η up to η^{N_1-1}; it can be seen that the left hand side of the kinematic boundary condition contains powers $\eta^{-(N_1-2)}$ through η^{N_1-2} (the multiplication by $\overline{z_s}$ contributing η^{-1}). Therefore, on the outer boundary, we equate the complex Laurent coefficients for powers up to $N_1 - 2$.

On each inner boundary m, the series for m for dz/dt contains powers of η down to η^{-N_m}; it can be seen that the left hand side of the kinematic boundary condition contains powers η^{-N_m-1} through η^{N_m+1}, the multiplication by $\overline{z_s}$ again contributing η^{-1}. Therefore, on inner boundary m, we equate the complex Laurent coefficients for powers up to $N_m + 1$.

Since the left hand side of the kinematic boundary condition is real, the negative Laurent coefficients on each boundary are redundant, as is the imaginary part of the zero coefficient. Therefore, we only use half the equations. For the outer boundary, we use the equations for powers 1 through $N_1 - 2$, plus the real part of the equation for the constant coefficient. For inner boundary m, we use equations for powers 1 through $N_m + 1$, plus the real part of the equation for the constant coefficient. This makes for a total of $2\sum_m N_m + 3M - 6$ real equations for the $2\sum_m N_m + 3M - 3$ real and imaginary parts of the unknowns.

Finally we choose to set $dz_{1,0}/dt$ and $\Im\{dz_{1,1}/dt\}$ to zero in order to fix the three real degrees of freedom associated with the Riemann mapping theorem. We find that this choice works well for all the examples shown below. This results in a linear system that is square and invertible, comprising $2\sum_m N_m + 3M - 6$ real equations and unknowns.

The sizes of the linear systems for the dynamic and kinematic boundary conditions are both determined by $\sum_m N_m$, the total number of coefficients in the series (18). By making use of FFTs, the entries in these systems can be calculated quickly. For simplicity, we solve the systems using Gaussian elimination. In our implementation, therefore, most of the computation time is spent on the $O((\sum_m N_m)^3)$ operations per time step required to solve the systems. However, it is possible that future implementations may gain a significant improvement in speed by using iterative methods.

9. Perimeters and areas

One advantage of working with a conformal mapping description of the time evolving domain is that subsidiary quantities can be readily computed to high accuracy (since, in essence, we have a formula to collocate as many points as we like on the domain boundaries). Many applications (including the application to MOF fabrication) require calculation of the perimeters of the boundaries of the fluid region. These can be calculated readily from knowledge of the conformal mapping at each time step. Again suppressing dependence on t, the perimeter of the boundary given by the image of $|\zeta - \delta_m| = q_m$ can be written as an integral in the ζ plane,

$$\Gamma_m = \oint \sqrt{dz\, d\overline{z}} = \pm \mathrm{i} q_m \oint_{|\zeta-\delta_m|=q_m} \frac{|z'(\zeta)|}{\zeta - \delta_m}\, d\zeta. \tag{20}$$

Likewise, many applications require calculation of the hole areas. The area inside a boundary is the special case $p = 0$ of the integral

$$S_m = \iint z^p\, dA = \frac{1}{2\mathrm{i}} \oint_{|\zeta-\delta_m|=q_m} z(\zeta)^p \overline{z(\zeta)} z'(\zeta)\, d\zeta, \tag{21}$$

where Stokes' theorem has been used to rewrite the integral as a line integral around the boundary. The complex center of mass of the fluid region can be obtained by evaluating the integral with $p = 1$ over all the boundaries and dividing by the fluid area.

10. Validation

In the tests and examples that follow, we simulate the evolution of regions of fluid containing compressible bubbles, whose pressures we take equal to the external pressure. We thus set all p_m to zero ($m = 1, \ldots, M$). All calculations shown

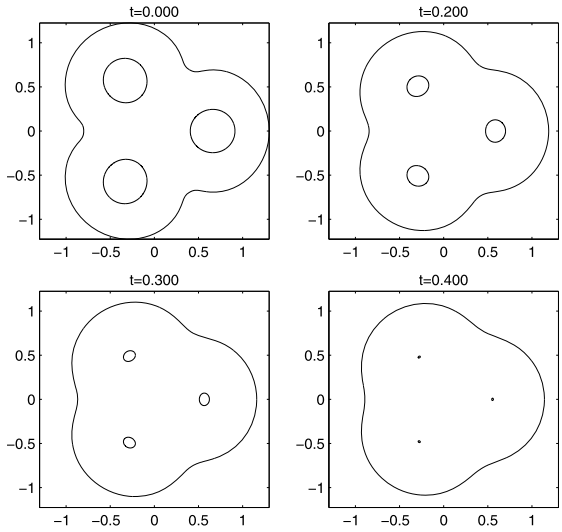

Fig. 2. Snapshots of the time evolution of the quadruply connected region described by Eq. (22). 25 coefficients were used for the $m = 1$ series; 10 coefficients were used for the $m = 2$, $m = 3$, and $m = 4$ series. A time step of 0.05 was used. The calculation took five seconds.

in this paper are performed using MATLAB on a computer with two 2.40 GHz Intel Pentium CPU's. Numerical parameters (numbers of coefficients and number of time steps) are selected to be reasonably low, and are checked for convergence with simulations at higher resolution. The initial configurations in most examples are normalized to have unit area.

Fig. 2 shows the evolution of a simple quadruply connected domain ($M = 4$). The upper left plot shows the image of the domain $|\zeta| \leq 1$, $|\zeta - 0.6e^{2\pi i m/3}| \geq 0.2$ ($m = 2, 3, 4$) under the initial map

$$z(\zeta, 0) = \zeta + 0.25\zeta^4 + 0.05\zeta^7, \tag{22}$$

which describes a rotationally symmetric fluid region with three near-circular bubbles. Under surface tension, the outer boundary becomes more circular and the holes shrink; after the holes have closed, and the domain has become simply connected, the calculation can be continued using the series associated with the outer boundary alone (results not shown). The simulation is executed with more coefficients than necessary to describe the initial configuration: 25 coefficients for the series associated with the outer boundary and 10 for the series associated with each inner boundary. The results are almost identical if no extra coefficients are used (just 8 for the outer boundary and 1 for each inner boundary). Using a time step of 0.05, the calculation took about five seconds. The key observation is that for smooth boundaries with non-pathological shapes (which, by the way, is often the case for MOFs) the method faithfully captures the evolution with very few coefficients.

An important quantitative validation of the numerical method is afforded by checking it against a family of known exact solutions for the two-dimensional sintering of $N \geq 3$ equal circular cylinders in a doubly connected annular arrangement [5]. These solutions are multiply connected generalizations of the example given in Kropinski [17] consisting of two cylinders. A summary of these solutions is given in Appendix C; they give closed form expressions for the time-evolving conformal map allowing us to check that the numerical method accurately retrieves the same results. For a given $N \geq 3$ the exact solutions depend on just 3 time-evolving parameters $\rho(t)$, $a(t)$ and $A(t)$ satisfying a known set of ordinary differential equations (given in the appendix). The fluid domain here is doubly connected so the conformal preimage region is taken to be the time-evolving annulus $\rho(t) < |\zeta| < 1$ where $\rho(t)$ must be dynamically determined.

A visual comparison between the numerical method and the exact solution is shown in Fig. 3 for $N = 10$. For this test, a configuration for close-to-touching cylinders characterized by regions of very high curvature and described by parameters $\rho(0) = 0.8100$ and $a(0) = 1.088$ (these values are taken from [5]) is first evolved using the exact solution in Appendix C for a time interval of 0.05. This provides us with an initial configuration for our numerical code shown in Fig. 3 (upper left plot), characterized by a curvature of about 450 where the cylinders meet. The evolution from this initial configuration was then obtained by both the exact solutions and the numerical method over the time interval $0.000 \leq t \leq 0.100$, using 1000 time steps and, for the numerical method, 500 coefficients for each of the two subseries. Snapshots are shown at two times (middle and lower plots). The numerical method captures the evolution faithfully, as is evident visually from the close-up plots in Fig. 3.

In Fig. 4, the numerical method is shown to converge to the exact solution as the number of coefficients is increased. The convergence is exponential, indicating spectral accuracy. Points on the two solutions' boundaries differ by an average of 10^{-15} at $t = 0.100$ when 500 coefficients are used. This is very efficient in the number of unknowns. For comparison, for the example with two cylinders, a configuration with comparable curvature, the boundary integral method described by Kropinski [17] requires 32768 boundary points to achieve errors of 10^{-5}. (It should be noted, of course, that the number of unknowns is not a direct measure of the computation time.)

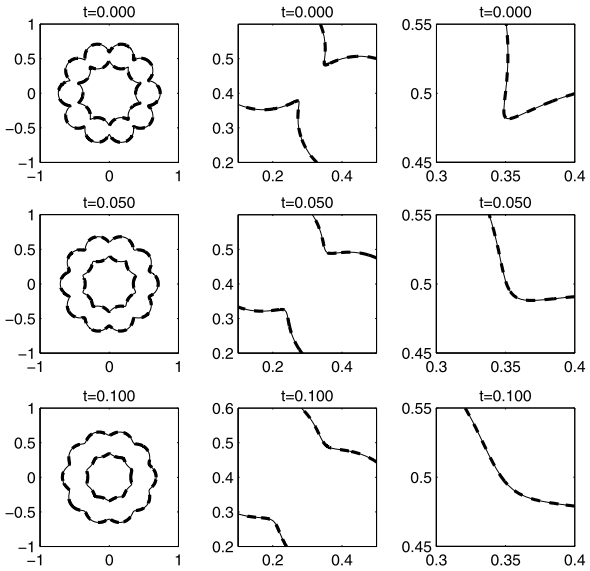

Fig. 3. Numerical solution (dashed) for the sintering of $N = 10$ circular cylinders overlaid with the exact solution from Appendix C (solid) at three different times. The configuration shown in the upper left plot was evolved using both the exact solution and the numerical method, giving configurations at two later times (middle and lower plots). Right-hand plots show closeups of a region of high curvature. This calculation required 1000 time steps and, for the numerical method, 500 coefficients for each subseries.

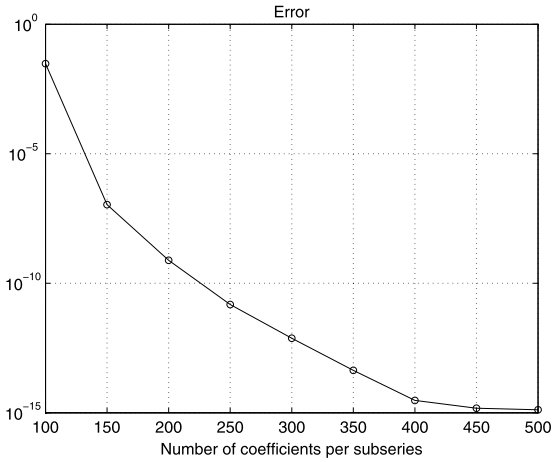

Fig. 4. Error in numerical solution for the example in Fig. 3 as the number of coefficients is varied. Error is the absolute difference in $z(\zeta, t)$ from the exact solution (Appendix C) at $t = 0.100$, averaged over equally spaced points ζ on the boundaries in the preimage plane.

Another validation is provided by a family of asymptotic solutions available for the evolution of the center-line of a thin annulus of fluid [10] (also a doubly connected fluid region). These solutions are valid provided the fluid region is sufficiently "thin". We calculated an asymptotic solution from Griffiths & Howell [10] for which a square with rounded corners is the final center-line shape (the solutions in [10] are obtained to understand an inverse problem arising in the manufacture of thin glass tubing). We then compared the asymptotic solution with the numerical solution computed using 100 coefficients for each series for $z(\zeta, t)$, $F(\zeta, t)$ and $G(\zeta, t)$. For our numerical scheme, the method of Kropf [16] was employed to obtain the required conformal map to the initial domain. The excellent agreement is evident in Fig. 5. Because our full solution requires fairly low computation time, the numerical method is practical for the evolution of a thin annulus, and could be used to extend solutions to the non-thin regime.

11. Examples

We now illustrate the use of the numerical method on several realistic examples arising in applications. Fig. 6 shows the evolution of a triply connected region initially characterized by thin walls. The relatively sharp corners necessitate a large number of coefficients, and a small time step in the early stages of the evolution, but the method works well. As the

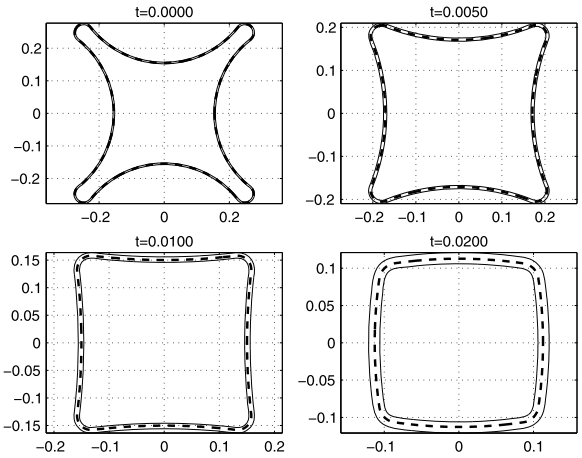

Fig. 5. Numerical solution (solid) for a thin fluid annulus whose center-line evolves into a square shape, overlaid with the center-line predicted by an asymptotic solution from Griffiths & Howell [10] (dashed) at several times. The numerical solution uses 100 coefficients on each boundary and a time step of 0.005. The calculation took 16 seconds.

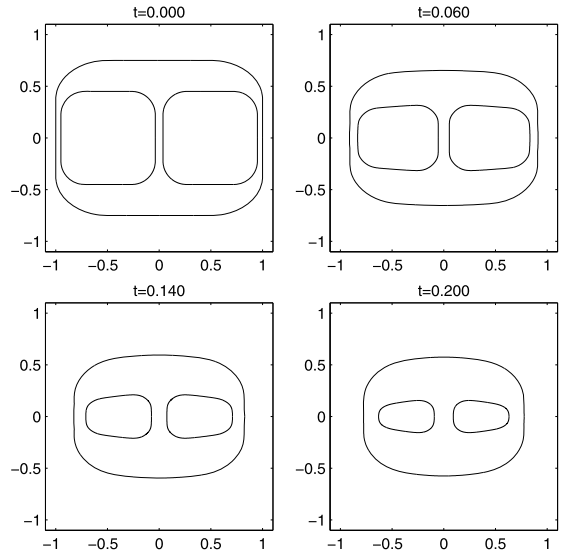

Fig. 6. Snapshots of the time evolution of a thin-walled, triply connected region. 50 coefficients were used for each series. A time step of 0.02 was used. The calculation took 23 seconds.

surface tension smoothes out high curvature regions under evolution, adaptive time-stepping could be used to optimize the calculations.

Since our work is motivated by the need to study the fibre drawing problem for microstructured optical fibres (MOFs), Fig. 7 shows results for the evolution of the cross section of a hypothetical MOF initially consisting of six closely-spaced triangular channels separated by thin threads of material. The proximity of the channels necessitates a fairly large number of coefficients (40 for each series in this example) but the calculation is still efficient. The initial conformal mapping for this example was constructed by seeding just the $q_j^2/(z-\delta_j)^2$ term in each of the series expansions in (18) about each channel which gives rise to the near triangular shape of the initial pores. The effect of surface tension is to cause the initially close-to-touching channels to shrink while simultaneously circularizing. The channels are close enough to the outer boundary in this example for the latter to develop a noncircular shape.

The geometrical microstructure of MOFs often comprises relatively large number of channels (of the order of 5 to 100, say). A typical cross-section of such a MOF is shown in Fig. 8 and consists of a hexagonal array of 54 small circular channels. Because the channels in the initial configuration are all circular, the initial conformal mapping from a circular preimage region is just the identity map $z(\zeta,0)=\zeta$ (shown here scaled to have unit area). The simulation here captures a feature commonly observed for MOFs of such a geometry: the channels along the inner-most ring tend to become extended along the azimuthal direction, while those at the corners of the hexagon on the outer-most ring become extended radially.

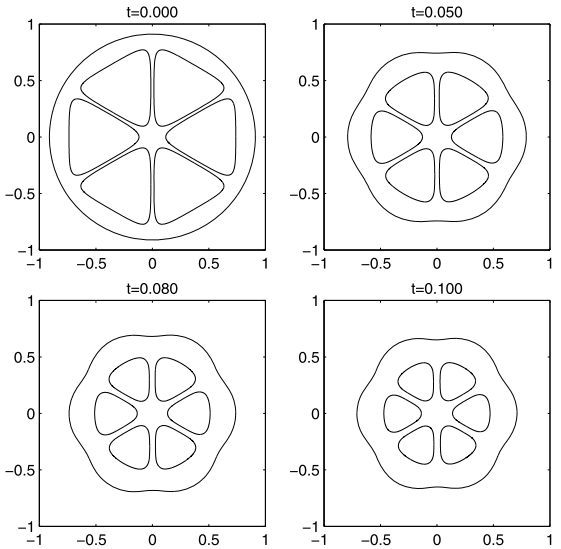

Fig. 7. Snapshots of the time evolution of an example MOF with six triangular channels separated by thin threads. 40 coefficients were used for each series. A time step of 0.002 was used. The calculation took about seven minutes.

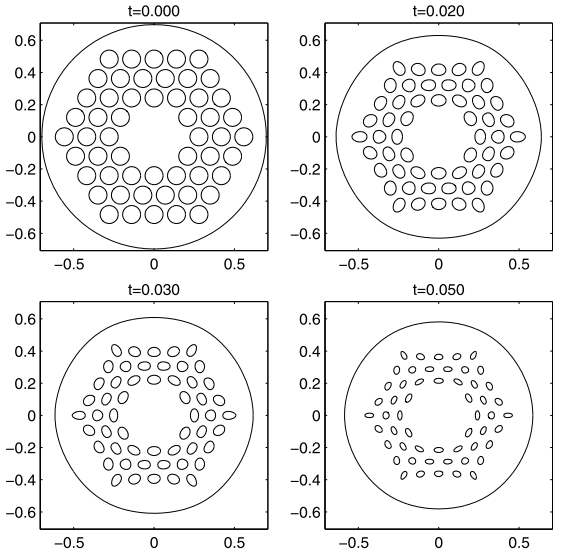

Fig. 8. Snapshots of the time evolution of an example MOF configuration with 54 initially circular channels. For this calculation, 10 coefficients were used for the $m = 1$ series and 3 coefficients were used for the other series. A time step of 0.01 was used. The calculation took 90 seconds.

It is worth emphasizing that, because our method represents shapes analytically, it is well suited to configurations of holes whose shapes possess some degree of rotational symmetry. Boundaries that can only be accurately described by a large number of collocation points can often be represented with a few coefficients. (Similarly, although we have not done so in our code, if MOFs that possess definite rotational symmetries are of specific interest, the symmetry can be used to dramatically reduce the number of unknown conformal mapping coefficients to be resolved by the simulation.) Fig. 9 shows a hypothetical MOF consisting of a circular array of channels that are approximately triangular. Similar to the example in Fig. 7 the initial configuration is the image of a circular domain under the initial conformal map

$$z(\zeta, 0) = \zeta - \sum_{m=2}^{M} 0.015 e^{3\mathrm{i}\arg(\delta_m)} (\zeta - \delta_m)^{-2} q_m^2, \tag{23}$$

scaled to have unit area. In alternative numerical schemes such as a boundary integral calculation, the triangles' sharp corners would necessitate a large number of points for proper resolution; in the present method, the initial subseries for each triangle requires only two coefficients, although to maintain accuracy, the calculation retained 10 coefficients for each

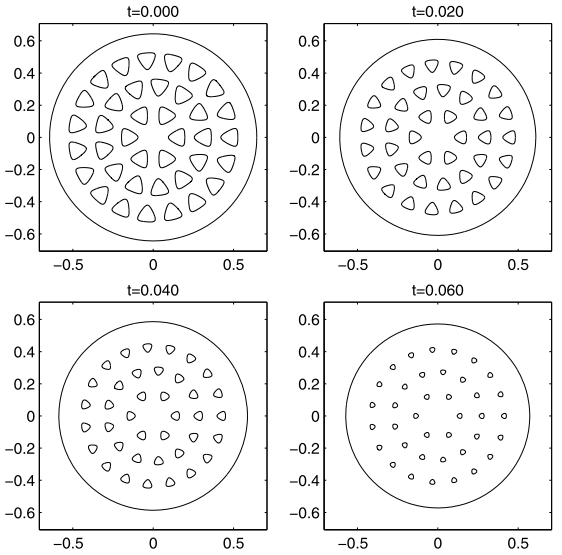

Fig. 9. Snapshots of the time evolution of an example MOF configuration with 38 triangular channels. The initial configuration is described by an explicit map (23). For this calculation, 10 coefficients were used for each subseries. A time step of 0.01 was used. The calculation took 176 seconds.

subseries. Even so, the evolution of this multiply connected region with sharp boundaries can be calculated quickly and accurately.

12. Discussion

The conformal mapping method described in this paper offers several advantages over competing methods for solving the two dimensional surface tension driven Stokes flow problem that we have tried to elucidate here. It is well suited to regions with regular arrays of holes which results in the need to track a small number of time-evolving coefficients (Figs. 2, 7, 8, 9) which makes it ideal for our motivating application – modelling the fabrication process for MOFs. The method can easily handle regions characterized by thin walls, although we expect numerical difficulties to arise when the preimages of the boundaries become too close in the ζ-plane. Our approach differs from previous methods [9,3] that use complex variable formulations in that we do not solve the Sherman–Lauricella integral equation. Moreover, previous treatments based on the Sherman–Lauricella integral equation do not generally employ conformal mapping descriptions of the free surfaces as we have done here.

If the method here has a possible drawback it is that if a specific initial domain is of particular interest then it is necessary to find the initial conformal mapping function $z(\zeta, 0)$ to that domain in the form (18). However the subject of numerical conformal mapping is well developed and many analytical and numerical resources exist for the construction of such maps (we have made use, for example, a Fornberg method for multiply connected domains [16]). We would argue that while this initial "set-up" step might appear burdensome (in comparison to, say, boundary integral methods) there are several attendant advantages for the evolution problem once that set-up has been made.

Data statement

This article presents details of a numerical method and all graphs can be reproduced by implementing this method.

Acknowledgements

This research is supported by the Engineering and Physical Sciences Research Council (EP/K019430/1) and the Leverhulme Trust (RPG-358). DGC acknowledges support from a Royal Society Wolfson Research Merit Award.

Appendix A. Elimination of redundancy in the dynamic boundary condition

Because the left hand side of the dynamic boundary condition satisfies (19), one of its real equations is redundant, and must be eliminated. This appendix gives the details, again suppressing dependence on t. With the expansions on each boundary given by

$$H(\zeta, \overline{\zeta}) - A_m = \sum_{n=-\infty}^{\infty} \hat{H}_{m,n} \eta^n, \qquad \eta^{-1} \overline{z'(\zeta)} = \sum_{p=-\infty}^{\infty} \chi_{m,p} \eta^p, \tag{A.1}$$

(19) gives a condition on the coefficients $\hat{H}_{m,n}$,

$$0 = \Re \sum_m \pm q_m \oint_{|\eta|=1} \eta^{-1} \left(\sum_{p=-\infty}^{\infty} \chi_{m,p} \eta^p \right) \left(\sum_{n=-\infty}^{\infty} \hat{H}_{m,n} \eta^n \right) d\eta \tag{A.2}$$

Only the η^{-1} terms contribute to the integral, giving a concise form of the condition on the $\hat{H}_{m,n}$,

$$0 = 2\pi \Im \sum_m \mp q_m \sum_n \chi_{m,-n} \hat{H}_{m,n},$$

or

$$0 = \sum_m \mp q_m \sum_n \left(\Im\{\chi_{m,-n}\}\Re\{\hat{H}_{m,n}\} + \Re\{\chi_{m,-n}\}\Im\{\hat{H}_{m,n}\} \right). \tag{A.3}$$

(A.3) gives explicitly the relationship between the real and imaginary parts of the coefficients of the left hand side of (9). Each real and imaginary part of a coefficient corresponds to an equation of the linear system for (9). To make the equations of this system independent, any equation given in (A.3) can be eliminated. We choose to eliminate the row $\Re\{\hat{H}_{m,n}\}$ or $\Im\{\hat{H}_{m,n}\}$ whose coefficient in (A.3) is largest in absolute value.

Appendix B. Solving the dynamic boundary condition for a circle

For a circle, $z(\zeta) = R\zeta$, where R is real. Expanding the dynamic boundary condition (9) in powers of ζ gives

$$\begin{aligned}
&\vdots \\
\zeta^3 :&\quad F_3 = 0 \\
\zeta^2 :&\quad F_2 = 0 \\
\zeta^1 :&\quad F_1 + \overline{F_1} = \tfrac{1}{2} + \tfrac{1}{2} p_1 R \\
\zeta^0 :&\quad F_0 + 2\overline{F_2} + \overline{G_0} - A_1 = 0 \\
\zeta^{-1} :&\quad 3\overline{F_3} + \overline{G_1} = 0 \\
\zeta^{-2} :&\quad 4\overline{F_4} + \overline{G_2} = 0 \\
&\vdots
\end{aligned} \tag{B.1}$$

The equations for ζ^2 and higher imply $F_2, F_3, \ldots = 0$. The equations for ζ^{-1} and lower imply $G_1, G_2, \ldots = 0$. This leaves only the equations for ζ^0 and ζ^1 to relate F_0, F_1, G_0, and A_1. To fix the ambiguity in the Goursat representation and the translational degree of freedom in the free boundary problem, we can set $F_0 = 0$ and $G_0 = 0$. The ζ^0 equation then implies that $A_1 = 0$ (recall that $F_2 = 0$). The single remaining equation is then

$$F_1 + \overline{F_1} = \frac{1}{2} + \frac{1}{2} p_1 R, \tag{B.2}$$

which provides one real constraint on the complex quantity F_1. Writing out its real and imaginary parts,

$$2\Re\{F_1\} = \frac{1}{2} + \frac{1}{2} p_1 R, \qquad 0 = 0. \tag{B.3}$$

The trivial second equation reflects the fact that a flow with a free boundary can never exert a net torque. The surface tension and pressure do not impose a torque – if they did, the right hand side of the second equation in (B.3) would be nonzero, and we would have an unsolvable equation. Because (B.2) has only one nontrivial part, it leaves undetermined the imaginary part of F_1. However, we still need to set the rotational degree of freedom in the free boundary problem, which we can do by imposing the condition $\Im\{F_1\} = 0$.

Appendix C. Analytical solution for sintering of circular cylinders

This appendix reviews the analytical solutions for the sintering of N equal circular cylinders [5] used in section 10 to test our numerical method. The solutions give the shape of the evolving fluid region $D(t)$ as the image of the time-evolving annulus $\rho(t) < |\zeta| < 1$ under the explicit conformal map

$$z(\zeta, t) = A(t) f(\zeta, t), \qquad f(\zeta, t) = \zeta \frac{P_N(\zeta \rho(t)^{2/N} a(t)^{-1}, \rho(t))}{P_N(\zeta a(t)^{-1}, \rho(t))}, \tag{C.1}$$

with

$$A(t) = \left[\frac{\hat{P}_N(1, \rho(t))}{\pi P_N(\rho(t)^{2/N}, \rho(t)) f'(a(t)^{-1}, t)} \right]^{1/2},$$

where a prime denotes the partial derivative with respect to ζ, $f'(\zeta, t) = \partial f(\zeta, t)/\partial\zeta$. N is the number of cylinders; in Fig. 3, we set $N = 10$. The functions $P_N(\zeta, \rho)$ and $\hat{P}_N(\zeta, \rho)$ are defined by

$$P_N(\zeta, \rho) \equiv (1 - \zeta^N) \prod_{k=1}^{\infty} (1 - \rho^{2kN} \zeta^N)(1 - \rho^{2kN} \zeta^{-N}), \qquad \hat{P}_N(\zeta, \rho) \equiv P_N(\zeta, \rho)/(1 - \zeta^N). \tag{C.2}$$

The above equations are reproductions of equations (2.16), (2.18) and (3.2) of [5]. The time-evolving parameters $\rho(t)$ and $a(t)$ satisfy the ordinary differential equations [5]:

$$\begin{aligned} \frac{d\rho}{dt} &= -\frac{\rho}{4\pi \mathrm{i}} \left(\oint_{|\eta|=1} \frac{d\eta}{\eta} \frac{1}{|z'(\eta, t)|} + \oint_{|\eta|=\rho} \frac{d\eta}{\eta} \frac{1}{\rho |z'(\eta, t)|} \right) \\ \frac{da}{dt} &= a I(a^{-1}, t), \end{aligned} \tag{C.3}$$

where, for brevity, we have suppressed the dependence of these parameters on t in our notation. These ordinary differential equations are solved numerically using the Runge–Kutta fourth-order method. The function $I(\zeta, t)$ is

$$I(\zeta, \tau) = I^+(\zeta, \tau) - I^-(\zeta, \tau) + C(\tau),$$

where

$$\begin{aligned} I^+(\zeta, \tau) &= \frac{1}{4\pi \mathrm{i}} \oint_{|\eta|=1} \frac{d\eta}{\eta} \left(1 - 2\frac{\zeta}{\eta} \frac{P_1'(\zeta/\eta, \rho)}{P_1(\zeta/\eta, \rho)} \right) \frac{1}{|z'(\eta, \tau)|}, \\ I^-(\zeta, \tau) &= \frac{1}{4\pi \mathrm{i}} \oint_{|\eta|=\rho} \frac{d\eta}{\eta} \left(1 - 2\frac{\zeta}{\eta} \frac{P_1'(\zeta/\eta, \rho)}{P_1(\zeta/\eta, \rho)} \right) \left[-\frac{1}{\rho |z'(\eta, \tau)|} - \frac{2}{\rho} \frac{d\rho}{d\tau} \right], \\ C(\tau) &= -\frac{1}{4\pi \mathrm{i}} \oint_{|\eta|=\rho} \frac{d\eta}{\eta} \left(-\frac{1}{\rho |z'(\eta, \tau)|} - \frac{2}{\rho} \frac{d\rho}{d\tau} \right). \end{aligned} \tag{C.4}$$

(Note that in these integrands z' is evaluated at η, not at ζ as indicated in [5].) All integrals around the circles $|\eta| = 1$ and $|\eta| = \rho$ are evaluated using the trapezoidal rule.

References

[1] L.K. Antanovskii, Boundary integral equations in quasisteady problems of capillary fluid mechanics, part 1: application of the hydrodynamic potentials, Meccanica 25 (1990) 239–245.
[2] P. Buchak, D.G. Crowdy, Y.M. Stokes, H. Ebendorff-Heidepriem, Elliptical pore regularisation of the inverse problem for microstructured optical fibre fabrication, J. Fluid Mech. 778 (2015) 5–38.
[3] S.S. Chakravarthy, W.K.S. Chiu, Boundary integral method for the evolution of slender viscous fibres containing holes in the cross-section, J. Fluid Mech. 621 (2009) 155–182.
[4] D.G. Crowdy, Compressible bubbles in Stokes flow, J. Fluid Mech. 476 (2003) 345–356.
[5] D.G. Crowdy, Viscous sintering of unimodal and bimodal cylindrical packings with shrinking pores, Eur. J. Appl. Math. 14 (2003) 421–445.
[6] L. Cummings, P.D. Howell, On the evolution of non-axisymmetric viscous fibres with surface tension, inertia and gravity, J. Fluid Mech. 389 (1999) 361–389.
[7] L. Cummings, S. Howison, J.R. King, Two-dimensional Stokes and Hele-Shaw flow with free surfaces, Eur. J. Appl. Math. 10 (1999) 635–680.
[8] G.M. Goluzin, Geometric Theory of Functions of a Complex Variable, American Mathematical Society, Providence, RI, USA, 1969.
[9] L. Greengard, M.C. Kropinski, A. Mayo, Integral equation methods for Stokes flow and isotropic elasticity in the plane, J. Comput. Phys. 125 (1996) 403–414.
[10] I.M. Griffiths, P.D. Howell, The surface-tension-driven evolution of a two-dimensional annular viscous tube, J. Fluid Mech. 593 (2007) 181–208.
[11] R.W. Hopper, Plane Stokes flow driven by capillarity on a free surface, J. Fluid Mech. 213 (1990) 349–375.
[12] T.Y. Hou, J.S. Lowengrub, M.J. Shelley, Removing the stiffness from interfacial flows with surface tension, J. Comput. Phys. 114 (1994) 312–338.
[13] P.R. Jagota, A. Dawson, Micromechanical modeling of powder compacts – I. Unit problems for sintering and traction induced deformation, Acta Metall. 36 (1988) 2551–2561.
[14] P.R. Jagota, A. Dawson, Simulation of the viscous sintering of two particles, J. Am. Ceram. Soc. 73 (1990) 173–177.
[15] J.C. Knight, Photonic crystal fibres, Nature 424 (2003) 847–851.
[16] E. Kropf, A Fornberg-like method for the numerical conformal mapping of bounded multiply connected domains, Master's thesis, Wichita State University, 2009.
[17] M.C.A. Kropinski, An efficient numerical method for studying interfacial motion in two-dimensional creeping flows, J. Comput. Phys. 171 (2001) 479–508.

[18] H.K. Kuiken, Viscous sintering: the surface-tension-driven flow of a liquid form under the influence of curvature gradients at its surface, J. Fluid Mech. 214 (1990) 503–515.
[19] W. Langlois, Slow Viscous Flow, Macmillan, 1964.
[20] N.I. Muskhelishvili, Some Basic Problems of the Mathematical Theory of Elasticity, Springer, 1977.
[21] R. Ojala, A. Tornberg, An accurate integral equation method for simulating multi-phase Stokes flow, J. Comput. Phys. 298 (2015) 145–160.
[22] C. Pozrikidis, Boundary Integral and Singularity Methods for Linearized Viscous Flows, Cambridge University Press, Cambridge, 1992.
[23] C. Pozrikidis, Expansion of a compressible gas bubble in Stokes flow, J. Fluid Mech. 442 (2001) 171–189.
[24] C. Pozrikidis, Computation of the pressure inside bubbles and pores in Stokes flow, J. Fluid Mech. 474 (2003) 319–337.
[25] A.R.M. Primo, L.C. Wrobel, H. Power, An indirect boundary-element method for slow viscous flow in a bounded region containing air bubbles, J. Eng. Math. 37 (2000) 305–326.
[26] S. Richardson, Two-dimensional slow viscous flows with time-dependent free boundaries driven by surface tension, Eur. J. Appl. Math. 3 (1992) 193–207.
[27] J.W. Ross, W.A. Miller, G.C. Weatherly, Dynamic computer simulation of viscous flow sintering kinetics, J. Appl. Phys. 52 (1981) 3884–3888.
[28] M. Siegel, Surfactant effects in steady, bursting and cusping bubbles in two-dimensional Stokes flow, SIAM J. Appl. Math. 59 (1999) 1998–2027.
[29] M. Siegel, Cusp formation for time-evolving bubbles in two-dimensional Stokes flow, J. Fluid Mech. 412 (2000) 227–257.
[30] Y.M. Stokes, P. Buchak, D.G. Crowdy, H. Ebendorff-Heidepriem, Drawing of micro-structured fibres: circular and non-circular tubes, J. Fluid Mech. 755 (2014) 176–203.
[31] S. Tanveer, G.L. Vasconcelos, Time-evolving bubbles in two-dimensional Stokes flow, J. Fluid Mech. 301 (1995) 325–344.
[32] G.A.L. van de Vorst, Integral method for a two-dimensional Stokes flow with shrinking holes applied to viscous sintering, J. Fluid Mech. 257 (1993) 667–689.
[33] G.A.L. van de Vorst, R.M.M. Mattheij, Numerical analysis of a 2-d viscous sintering problem with non-smooth boundaries, Computing 49 (1992) 239–263.
[34] G.A.L. van de Vorst, R.M.M. Mattheij, H.K. Kuiken, A boundary element solution for two-dimensional viscous sintering, J. Comput. Phys. 100 (1992) 50–63.